Examination of Morphological Change of Active Materials for Solution-based Rechargeable Fluoride Shuttle Batteries using *In Situ* Electrochemical Atomic Force Microscopy Measurement

Ken-ichi Okazaki[*,†], *Hirofumi Nakamoto*[†], *Toshiro Yamanaka*[†], *Toshiharu Fukunaga*[†], *Zempachi Ogumi*[†], *and Takeshi Abe*[‡]

[†] Office of Society-Academia Collaboration for Innovation, Kyoto University, Gokasho, Uji 611-0011, Japan

[‡] Graduate School of Engineering, Kyoto University, Nishikyo-ku, Kyoto 615-8510, Japan.

ABSTRACT: Batteries using fluoride anion as the carrier might possess high capacity and energy density. Especially, the fluoride shuttle battery (FSB), which uses a fluoride ion-conductive liquid

electrolyte and operates at room temperature, has been reported previously and is deemed a solution to the global energy and environmental crises. Although several electrolyte solutions have been synthesized, and the fluorination/defluorination reactions of various active materials have been evaluated, no subsequent FSBs using those electrolyte solutions have been reported. In this study, two metal species, Bi and Pb, which have different fluorination/defluorination mechanisms in the electrolyte solution composed of alkylammonium fluoride and an ionic liquid, were used as the positive and negative active materials for the FSB. The fluorination/defluorination mechanisms at each electrode during the reactions were explained by *in situ* electrochemical atomic force microscopy (EC-AFM) measurement. Difference in the morphological changes by two existing mechanisms, direct fluorination and dissolution–deposition, were clarified with evidence. Furthermore, the charge/discharge process of the FSB, with the electrolyte solution combining the active materials, was demonstrated, and the cycling performance and capacity fading mechanism were discussed based on the characteristic morphological change of the active materials at their interface with the electrolyte solution obtained by *in situ* EC-AFM measurements.

1. INTRODUCTION

Rechargeable batteries with high energy densities, long lifespans and service life have been required for battery electric vehicles (BEVs), hybrid electric vehicles (HEVs), drones, mobile devices, and other applications.[1-4] In addition, energy-dense batteries are crucial for protecting the environment and building unperturbed large-scale energy storage devices for fluctuating renewable energy sources, such as wind and solar power.

Recently, energy-dense batteries based on anion transfer, such as chloride and fluoride have garnered research interest because they can be fabricated by selecting the appropriate active materials for the positive and negative electrodes.[5-9] Especially, rechargeable batteries based on a fluoride shuttle (fluoride shuttle batteries; FSBs) have emerged as a candidate with remarkably better storage capacity than chloride and even other current batteries.[10-12] For example, the theoretical gravimetric discharge capacities of FSBs based on the conversion reaction of metal-fluoride/metal combinations of BiF_3, CuF_2, and FeF_3 are to be 302, 528, and 712 mAh/g, respectively, for positive electrode materials. “Fluoride shuttle” refers to the reversible transfer of fluoride ions from one electrode to the other via solid or liquid electrolyte depending on whether the battery is being charged or discharged.

In all-solid FSBs, fluoride ions apparently transferred between the positive and negative electrodes through a fluoride ion-conductive solid electrolyte, and then some metal fluoride and the corresponding metal are reversibly produced at each electrode.[13-18] Significantly advanced all-solid FSB was fabricated by Anji Reddy and Fichtner a decade ago, and the all-solid FSB operated at elevated temperatures.[14] Most investigations into all-solid FSBs were performed at temperatures greater than 423 K, while a few have demonstrated their performance at room temperature in recent.[18-20]

Meanwhile, in FSBs with electrolyte solutions, the fluoride species in the solution are reserved and must reversibly react with metal or metal fluoride at both the positive and negative electrodes during the charge and discharge cycle. That is, fluorination and defluorination must occur simultaneously at both electrodes. The literature contains few reports on the fabrication of FSBs using liquid electrolytes. To the best of the authors' knowledge, Darolles *et al.* were the first to describe such an FSB in US patent.[21-22] However, they could not produce strong evidence for the fluoride shuttle phenomenon. Later, Gschwind *et al.* investigated BiF_3/Li and BiF_3/Mg electrode systems with fluoride ion-conducting electrolyte based on a polyethylene glycol polymer and an ammonium bi-fluoride salt at room temperature.[23] However, these systems might not be

rechargeable because they can only be discharged (i.e., the defluorination of metal fluoride at the positive electrode) and consequently display poor reversibility. In a previous study, we demonstrated the reversible charge and discharge reactions of an FSB with an electrolyte solution containing alkylammonium fluoride at room temperature.[24] However, its capacity faded immediately, and therefore the utilization and cyclability of its active material needs to be improved.

After our demonstration of the FSB, other studies have produced a few novel electrolyte solutions containing fluoride species, and have investigated the fluorination/defluorination reactions of active materials, such as Cu, Bi, and Pb, using a three-electrode cell with an auxiliary electrode such as Pt.[25-33] Electrolytes, solvents, or additives might disintegrate fatally on the surface of the auxiliary electrode in order to keep the current density equal to the fluorination/defluorination reaction of the active material in those systems. Therefore, few studies have practically demonstrated the fluoride shuttle phenomenon between the positive and negative electrodes, i.e., charge and discharge of FSBs, with their electrolyte solution.

One of the reasons for less demonstration is that the progression of dissolution of the active metal species was concerned in addition to the anticipated direct fluorination process. Similarly,

in the defluorination process of most studies, the active metal fluoride had dissolved and then its reducing product deposited on the electrode, instead of direct defluorination. Thus, the mechanism becomes complex depending on the combination of the metal/metal fluoride species and the type of the electrolyte solution. For example, Bi undergoes direct fluorination in the electrolyte solution composed of alkylammonium fluoride and TMPA-TFSA; however, the defluorination reaction of BiF_3 strongly depends on its crystal system.[34-35] The study reported two pathways—direct defluorination and dissolution followed by reductive deposition.[35] Another study suggested that the electrolyte, containing an anion receptor such as fluorobis(2,4,6-trimethylphenyl)borane, first dissolved and then reductively precipitated Bi.[26] Such an anion receptor had already improved cyclability in FeF_3-based lithium-ion battery via dissociate and dissolve LiF, the discharge-product, into its electrolyte solution.[36] In the example for Cu, the dissolution of CuF_2 or Cu occurs as a main- or side-reaction of the defluorination or fluorination processes in two electrolyte solution systems—one containing fluorohydrogenate ionic liquids[29,32] and another fluorinated ether.[25] In the latter, dissolution proceeds in the same manner as with many other metal species; therefore, a yoke-shell structure in which the active material is surface-modified with a fluoride ion-conductive material in order to suppress the dissolution must be designed.[25]

In this study, two metal species, Bi and Pb, which have different fluorination/defluorination mechanisms in the electrolyte solution composed of alkylammonium fluoride and TMPA-TFSA, were used as the positive and negative active materials. The fluorination/defluorination mechanisms at each electrode during the reaction were explained by *in situ* electrochemical atomic force microscopy (EC-AFM) measurement. Furthermore, the charge/discharge process of the FSB, with the electrolyte solution combining the active materials, was demonstrated, and the cycling performance and capacity fading mechanism were discussed.

2. EXPERIMENTAL PROCEDURE

2.1 Synthesis of fluoride-containing electrolyte solutions

Electrolyte solutions containing fluoride ions were prepared by dissolving alkylammonium fluoride in an ionic liquid (IL). Tetramethylammonium fluoride (TMAF; Sigma-Aldrich) and 1-methyl-1-propylpiperidinium fluoride (MPPF; Tokyo Chemical Industry) were used as sources of fluoride ions. TMAF was used without further purification. MPPF, however, was purified by dissolving and drying it in acetonitrile containing molecular sieves, and recrystallizing it from 1,2-dimethoxyethane. Next, TMAF and purified MPPF were separately dissolved in IL, *N*,*N*,*N*-trimethyl-*N*-propylammonium bis(trifluoromethanesulfonyl)amide (TMPA-TFSA, Kanto

Chemical) in molar ratios of 1:50 and 1:10. The concentration of MPPF in the electrolyte solution was 0.08 mol/dm^3 for 1:50 and 0.38 mol/dm^3 for 1:10, respectively. Furthermore, a concentrated electrolyte solution with a concentration of 0.54 mol/dm^3 (MPPF:TMPA-TFSA = 1:7) was also prepared, to compare their conductivities.

2.2 Characterization of the electrolyte solutions

The electrochemical voltage window of MPPF/TMPA-TFSA was determined by cyclic voltammogram (CV) using a two-compartment H-shaped cell (VB10, EC Frontier Co., Ltd., Japan), in which the counter compartment is separated from the working electrode (WE) and reference electrode (RE) via a glass filter. A Pt wire (purity: 99.999%; Nilaco Corporation) was used as the WE, and a Li wire (diameter: 1 mm; Honjo Chemical Corporation), immersed in a 1-mol/dm^3 $LiPF_6$ / ethylene carbonate (EC) and dimethyl carbonate (DMC) mixed solvent (EC:DMC; 1:1 v/v, lithium battery grade, Kishida Chemical) as a quasi-RE ("quasi-Li"). Quasi-Li was separated from the measuring electrolyte solution via a vycor glass. The counter compartment was composed of a Li wire as the counter electrode (CE) immersed in 1-mol/dm^3 $LiPF_6$ / EC:DMC, to suppress the disintegration of the measuring electrolyte solution at the surface of the CE. The ionic conductivities of the three concentrations of MPPF/TMPA-TFSA were

determined by AC impedance measurements with Au-plated electrodes in the frequency range of 1 Hz to 100 kHz at 298 K. The temperature was controlled from 283 to 333 K in increments of 10 K by a thermostatic oven (SU-241, ESPEC Corp., Japan). The ^{19}F NMR spectra were acquired by a Bruker Avance III spectrometer at 296 K.

2.3 Preparation of BiF_3/C composite electrode

The BiF_3/C composite electrode was fabricated as follows. Anhydrous BiF_3 powder (purity: 99.9%) was purchased from Kojundo Chemical Laboratory and used after drying it at 473 K for two hours in vacuum. Acetylene black (AB, Denka Black, Denka Company Limited) was dried at 873 K for two hours in an Ar atmosphere. The anhydrous BiF_3 powder was mixed with AB in the weight ratio of 80:10, and the mixed powder was poured into a stainless-steel container with a ZrO_2-grinding bowl in an Ar atmosphere. Next, it was ball-milled at 600 rpm for six hours using a planetary ball mill (Premium line P-7, Fritsch). An aliquot of the as-prepared BiF_3/AB powder and polyvinylidene difluoride (PVDF) / *N*-methyl-2-pyrrolidone (NMP) solution (KF polymer, Kureha Corporation) was mixed using a planetary centrifugal mixer (THINKY). The resulting slurry was cast with a baker-type applicator (Hohsen Corporation) on a piece of Ti foil as a current

collector. The resulting BiF_3/C composite electrode (BiF_3:AB:PVDF = 80:10:10) was dried at 373 K for at least one night in vacuum to remove NMP.

2.4 Electrochemical measurements of Bi and Pb

Electrochemical measurements except the charge–discharge test for the FSB using the BiF_3/C composite were performed using either a three- or two-electrode beaker-type cell, and all measurements were performed at room temperature in a glove box filled with purified dry Ar gas (dew point <190 K). A Bi needle (diameter: 1.5 mm, 99.998%; Alfa Aesar) was used as the WE and positive electrode. Its surface area was estimated to be 0.16 cm^2. The oxidized surface layer of the Bi electrode was polished before use. A Pb wire (diameter: 1 mm) and plate (thickness: 1 mm) were purchased from Nilaco and used as the WE and CE after scraping off the oxidized surface layer. A surface-fluorinated Pb plate was used as CE or RE. The surface of the pristine Pb plate (99.999%, Nilaco) was electrochemically fluorinated in an electrolyte solution (TMAF/TMPA-TFSA or MPPF/TMPA-TFSA (1:50)). The amount of PbF_2 on the surface was controlled by an applied charge during the fluorination reaction of Pb. Hereafter, the PbF_2-deposited Pb electrode is denoted by Pb|PbF_2.

The reversible fluorination/defluorination reaction of Pb in TMAF/TMPA-TFSA or MPPF/TMPA-TFSA was performed at room temperature using Pb|PbF_2 as both the CE and RE. Furthermore, quasi-Li was used as the RE for the fluorination/defluorination of Pb to determine the potential difference between quasi-Li and Pb|PbF_2. Cyclic voltammetry was conducted at a scan rate of 1.0 mV/s. To confirm the crystal structure of fluorinated Pb, the electrochemical potentials of the electrodes were maintained at +0.05 V or +0.2 V *versus* Pb|PbF_2 for 12 hours, and then subjected to XRD measurements in an inert atmosphere, after adequately washing the electrodes in acetonitrile (lithium battery grade, Kishida Chemical). Galvanostatic charge–discharge tests of the FSB composed of Bi and PbF_2 were performed between 0 and +0.6 V, with charge and discharge currents of 31.0 and 15.5 μA/cm^2, respectively. The tests were conducted with and without cut off at 0.1 mAh within the charge capacity, and then repeated for 10 cycles. In this test, Pb|PbF_2 electrodes with varying PbF_2 capacity, i.e., the capacity of fluoride species, were prepared as the negative electrode. The capacity was controlled from zero to 1.0 mAh.

2.5 Charge–discharge measurement of BiF_3–Pb FSB system

The FSB with the BiF_3/C composite was subjected to a charge–discharge test using a flat-type cell (SB2A, EC Frontier Co., Ltd.). A positive electrode disk was punching out from the BiF_3/C

composite electrode, with a projected area of 1.33 cm^2. The FSB cell was prepared from the BiF_3/C composite disk, with a Pb disk (1.77 cm^2) as the negative electrode, two sheets of polypropylene separator (thickness: 50 μm), and 200 μL of MPPF/TMPA-TFSA (1:10) electrolyte solution. The FSB cell was assembled and measured at room temperature in a glove box filled with purified dry Ar.

The FSB was subjected to a galvanostatic charge–discharge test in the voltage range of 0–0.6 V with charge and discharge current densities of 7.5 and 3.8 μA/cm^2, respectively. Furthermore, the constant current constant voltage (CCCV) method was used for the first discharge process of the BiF_3–Pb FSB, because the protocol can demonstrate the reactivity of the BiF_3/C positive electrode and reveal the products after fully-discharge and following charge processes. First, the FSB was discharged at a constant current of *C*/100 rate, until the battery terminal voltage reached a cut-off value of 0.05 V. Then, a constant voltage mode was applied until the discharge current reached a cut-off value of *C*/500. After allowing it to idle for 30 min, the FSB was charged in the CC mode at *C*/100 rate, until the terminal voltage reached 0.6 V. The FSB cells were disassembled at three points: the end of CC discharge, full discharge (CCCV discharge), and subsequent CC charge. The

crystal structures of the Bi species in the disassembled BiF_3/C positive electrodes were revealed through XRD in an inert atmosphere.

2.6 In situ electrochemical atomic force microscopy measurement

The morphological changes of Bi and Pb during fluorination/defluorination were investigated via *in situ* electrochemical atomic force microscopy (EC-AFM) measurements using an airtight three-electrode EC cell (Asylum Research, Oxford Instruments). The *in situ* EC-AFM setup is illustrated as Figure S1 in Supporting Information. Bi and Pb plates were used as the WE after sequentially scrapping off the oxidized surfaces with emery paper #600 and rapping papers #1,000 and #10,000, and the area contacting the TMAF/TMPA-TFSA (1:10) electrolyte solution was regulated to 0.38 cm^2 via a PEEK cover. A Pb|PbF_2 wire and a graphite block were used as the RE and CE, respectively. The EC cell was assembled in an Ar-filled glove box. Pb was subjected to galvanostatic fluorination from 0 to +0.3 V *versus* Pb|PbF_2, with a current density of 52.6 μA/cm^2. Meanwhile, Bi was subjected to galvanostatic fluorination from +0.3 to +0.7 V, with a current density of 13.2 μA/cm^2. The tapping-mode *in situ* AFM images were collected on MFP-3D Origin (Asylum Research, Oxford Instruments) using a silicon nitride probe tip with a spring constant of 0.32 N/m. Sequential *in situ* AFM images were acquired in both top-down and bottom-up

directions at 682 or 341 seconds per image for Bi and 341 seconds per image for Pb, respectively. Movies during fluorination/defluorination were composed of the consecutive images in both directions.

2.7 Instrumentation

Most electrochemical measurements were performed using a VSP-300 multichannel potentiostat/galvanostat with a low-current-density probe (BioLogic Instruments). Conductivities of the electrolyte solutions were measured using an SI1287 electrochemical interface, 1255B frequency response analyzer, and impedance/gain-phase analyzer (Solartron Analytical). ^{19}F-NMR was measured with Avance III 600 (Bruker) using a 5-mm TCI CryoProbe. The morphologies of the fluorinated/defluorinated Bi and Pb were observed by field emission scanning electron microscopy (FE-SEM; SU-6600, Hitachi). Paired with FE-SEM, energy-dispersive X-ray spectroscopy (EDS) was performed using an EX-350x-act (HORIBA, Japan) at an accelerating voltage of 20 kV. The crystal structures of the fluorinated/defluorinated electrodes were identified using XRD (D8 ADVANCE, Bruker AXS K.K.) under Cu–Kα radiation (λ = 1.5418 Å) in an inert gas atmosphere. *In situ* EC-AFM measurement was performed using MFP-3D-Origin (Asylum

Research, Oxford Instruments), under electrochemical control using SP-240 potentiostat/galvanostat with a low-current-density probe (BioLogic).

3. RESULTS AND DISCUSSION

The fluoride-ion-containing liquid electrolyte was prepared by dissolving organic fluoride, such as MPPF, in an ionic liquid (TMPA-TFSA). Figure 1(a) illustrates the CV of the MPPF/TMPA-TFSA (1:50) electrolyte solution with Pt as the WE. This electrolyte solution was stable for 2.5 V from 1.0 to 3.5 V *versus* quasi-Li, and no noticeable current, such as that due to the hydrogen evolution reaction, was detected in this region. The fluorination/defluorination potential of Pb, i.e., Pb|PbF_2, determined from the Gibbs free energy was +2.49 V *versus* Li/Li^+. The potential difference between quasi-Li and Pb|PbF_2 was estimated to be 2.3 V, considering both anodic and cathodic decomposition potentials of the electrolyte solution. Therefore, this electrolyte solution was stable in the potential from -1.3 V to +1.2 V *versus* Pb|PbF_2.

Figure 1(b) depicts the ionic conductivities of MPPF/TMPA-TFSA with varying concentrations. The ionic conductivities of the electrolyte with concentrations of 0.08, 0.38, and 0.54 mol/dm^3 were 3.0, 2.5, and 2.3 mS/cm, respectively, at 298 K. These conductivities were contributed by whole ionic species, $TMPA^+$, $TFSA^-$, and the dissociated cation and anion from MPPF; therefore,

the major species contributing to the conductivities were the former two ionic species. MPPF was thermally unstable at relatively high temperatures, such as 333 K; consequently, the conductivity of the concentrated solution would have surged at this temperature. In contrast, the ionic conductivities decreased with increasing electrolyte concentration below 313 K, because the viscosities of the solutions increased.

Figure 1(c) illustrates the ^{19}F-NMR spectra of MPPF/TMPA-TFSA and TMAF/TMPA-TFSA. All the electrolyte solutions displayed extremely strong peaks at -79.8 ppm and a feeble one at approximately -140 ppm. The former was assigned to the CF_3 group in $TFSA^-$ and the latter to poly(hydrogen fluoride) species, $(HF)_nF^-$, respectively. The latter peak was contributed by the presence of a small amount of H_2O in TMPA-TFSA, i.e., the Hofmann elimination.[37-38] However, the relative amount of $(HF)_nF^-$ species was considerably small and did not depend on the fluoride sources, MPPF and TMAF or their varying concentrations. Therefore, $(HF)_nF^-$ must have originated from the small amount of water in the TMPA-TFSA solvent. Moreover, no significant difference was observed between the well-dehydrated MPPF and TMAF in the following electrochemical fluorination/defluorination behavior of Bi and Pb. Meanwhile, the peaks observed at -82 and -96 ppm were attributed to TMA-F and MPP-F, respectively. These spectra indicate that

the alkylammonium fluorides were sparsely dissociated in TMPA-TFSA, i.e., the chemical shifts of fluoride ions strongly depend on the original fluoride sources, TMA-F and MPP-F, and were largely reserved as a state similar to a molecular state in the solvent. Consequently, a small amount of the dissociated fluoride ions contributed to the fluorination of the active materials.

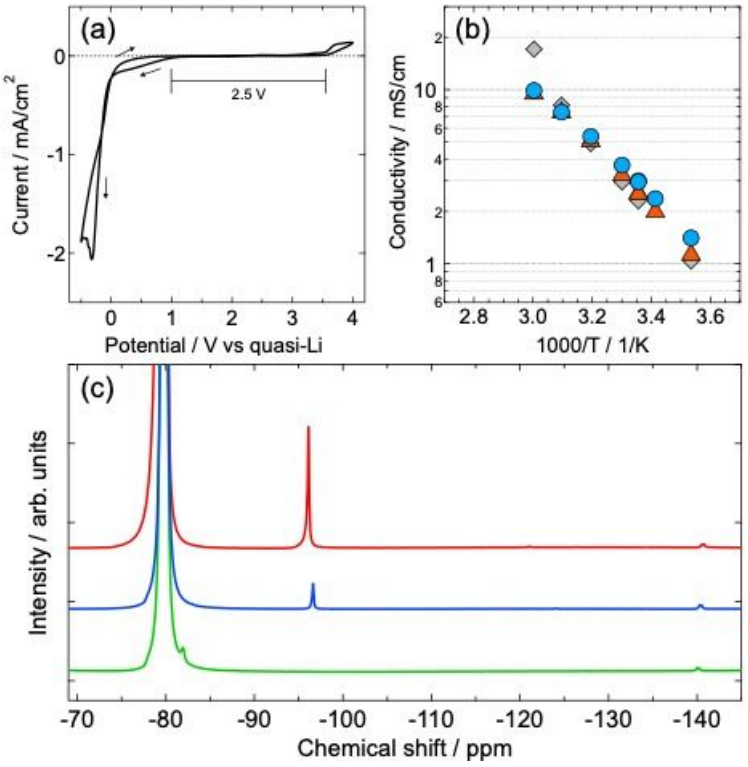

Figure 1. (a) Cyclic voltammogram (CV) of 0.08-mol/dm^3 MPPF/TMPA-TFSA as the electrolyte solution (1:50 molar ratio) at a scan rate of 1 mV/s. (b) Arrhenius plots for the ionic conductivity of the MPPF/TMPA-TFSA electrolyte solution in varying concentrations: 0.08 (circles), 0.38 (triangles), and 0.54 mol/dm^3 (diamonds), respectively. (c) ^{19}F-NMR spectra of the electrolyte

solutions: 0.38-mol/dm^3 MPPF/TMPA-TFSA (red), 0.08-mol/dm^3 MPPF/TMPATFSA (blue), and 0.08-mol/dm^3 TMAF/TMPA-TFSA (green).

Figure 2(a) illustrates the CV of Pb in MPPF/TMPA-TFSA at 298 K. The figure reveals two anodic peaks and one cathodic peak. The curve remained unchanged during five cycles of the CV measurement. This result implies that Pb can be reversibly oxidized and reduced in the electrolyte solution. To reveal the oxidized product, the potential of the Pb electrode was maintained at +0.05 V (first anodic peak) and +0.2 V (second one) *versus* Pb|PbF_2 for 12 h. Figure 2(b) displays the XRD patterns of the obtained oxidized Pb electrodes. For comparison, the XRD patterns of cubic Pb (Card no. 00-004-0686) and cubic-PbF_2 (Card no. 01-077-1865) are also illustrated in the figure. The XRD pattern of oxidized Pb at +0.05 V approximately corresponded to that of cubic Pb, except for the peak of PbO at $2\theta = 28°$. This result suggests that the first anodic peak in the CV corresponded to the oxidative dissolution of Pb in the electrolyte solution. In contrast, the XRD pattern of oxidized Pb at +0.2 V was attributed to cubic PbF_2, in addition to original cubic Pb. That is, the fluorination of Pb to PbF_2 occurred after oxidative dissolution.

These CV and XRD results indicate that Pb can be fluorinated and defluorinated reversibly. Figure 2(c) and (d) illustrate the SEM images of the surface of the fluorinated Pb plate. PbF_2

crystals had formed at arbitrary position of the flat Pb plate. Figure S2(a) displays the EDS spectra at the points corresponding to the SEM image in Figure S2(b). As a marked amount of F was detected on the crystal via the EDS spectra, the crystals were verified to be PbF_2. Figure S3 displays the other magnified SEM image of the same fluorinated Pb electrode, which indicates that the PbF_2 crystals grew not only onto the solution side, but also into the Pb plate. In a previous study, we reported an SEM observation upon the fluorination of Bi plate, and all the surfaces of Bi have been fluorinated uniformly.[24] Therefore, the present behavior of Pb is quite different from the fluorination mechanism of Bi. Deference of the fluorination mechanism between Pb and Bi is described in detail later.

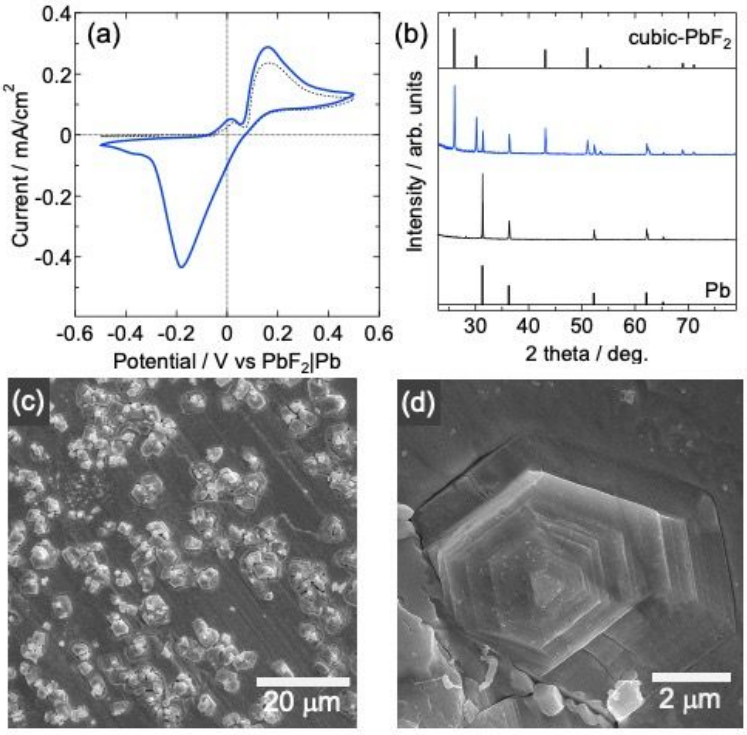

Figure 2. (a) CV of Pb in 0.08-mol/dm^3 MPPF/TMPA-TFSA. (b) XRD patterns of Pb electrodes after fluorination at 0.05 and 0.2 V *versus* Pb|PbF_2. (c, d) SEM images of the surface of Pb after fluorination.

With the Pb plate as a negative electrode, we investigated the charge–discharge reaction of the BiF_3-Pb FSB cell in MPPF/TMPA-TFSA at room temperature. Figure 3(a) displays the charge–discharge profile of the FSB cell. First, the cell was discharged to 0.05 V with a constant current (2) and then further discharged with a constant voltage until the current had decreased to *C*/500 (3). Subsequently, the cell was charged until 0.6 V in the CC mode at *C*/100 rate (4). The discharge capacities of the BiF_3/C positive electrodes with the CCCV mode neared the theoretical capacity of BiF_3, 302 mAh/g, and the subsequent recharge capacity was 235 mAh/g (78%). Figure 3(b) illustrates the XRD patterns of the BiF_3/C composite positive electrodes obtained at the initial state (1), end of CC discharge (2), full discharge (3), and subsequent CC charge (4).

In the initial state, the crystal structure of BiF_3 was a mixture of h–BiF_3 and o–BiF_3, because the BiF_3/C composite was prepared by ball-milling for a few hours, as depicted in Figure S4. After CC discharge (2), a peak was observed at 27.3° of Bi. Notably, the diffraction peaks of h–BiF_3 and o–BiF_3 disappeared, and instead those of c–BiF_3 appeared at the end of the CC discharge to 0.05

V (2). Yamanaka *et al.* reported the deference in reactivity and defluorination mechanism between orthorhombic and cubic BiF_3 in an MPPF/TMPA-TFSA electrolyte solution using *in situ* Raman microscopy.[35] In the study, o–BiF_3 discharged at a higher voltage than c–BiF_3 in the electrolyte solution to form Bi. Importantly, they found that o–BiF_3 had partially transformed into c–BiF_3 and then defluorinated at a lower voltage. Similarly, the as-obtained XRD patterns after CC discharge and full discharge of the BiF_3/C positive electrodes (Figure 3(b)) conformed with the *in situ* Raman measurement results. The subsequent charge reaction (refluorination) caused the disappearance of Bi and the formation of c–BiF_3. These results proved that, with Pb as the negative electrode, the BiF_3/C composite positive electrode underwent reversible defluorination/fluorination in the electrolyte solution at room temperature.

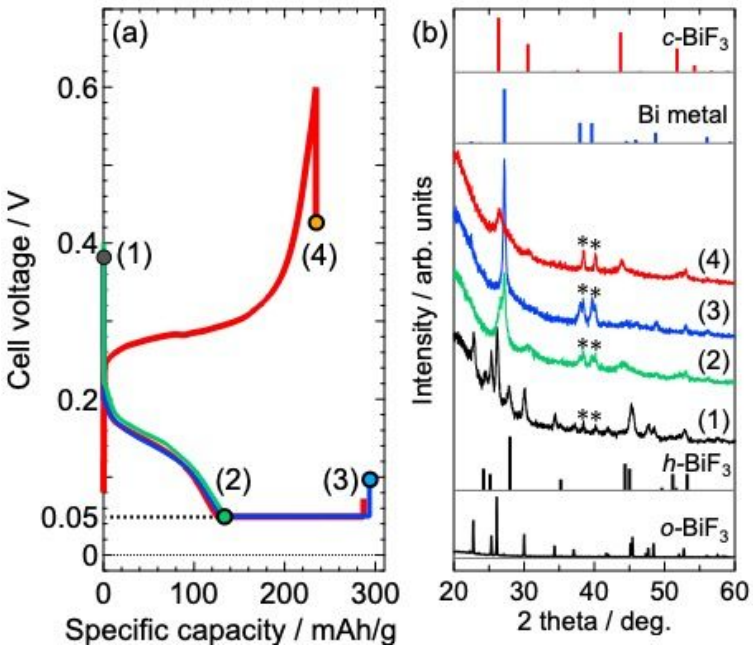

Figure 3. (a) Charge–discharge curves of BiF_3–Pb FSB with 0.08-mol/dm^3 MPPF/TMPA-TFSA as the electrolyte solution. The discharge process is switched to the constant voltage mode at 0.05 V. (b) XRD patterns of BiF_3/C positive electrodes after discharge and charge cycles. The numbers with parentheses and colors correspond to those in the charge–discharge curves (a). Asterisks (*) are the peaks of Ti as the current collector.

Figure 4(a) illustrates the charge reaction in the Pb|PbF_2–Bi FSB cell with Pb|PbF_2 as the negative electrode and Bi as the positive electrode. The charge–discharge profile and cyclability of the FSB cell with respect to the capacity of PbF_2 at the surface of the Pb negative electrode in the Pb|PbF_2–Bi FSB system were investigated. The obtained charge–discharge profiles are

depicted in Figure 4(b)–(e). The electrochemical measurement was limited at 0 V for discharge and +0.6 V for charge. The electrolyte solution was stable up to approximately +1.2 V *versus* Pb|PbF_2 (Figure 1(a)). It is not so important for the Bi positive electrode to charge beyond +0.6 V; therefore, we limited there to prevent the anodic dissolution of the metal at higher voltages.

In addition, the cycling performance of the Bi positive electrode was evaluated with a charge capacity limit of 0.1 mAh. The reason for limiting the capacity is that BiF_3, the charge product at the surface of Bi, has poor electronic and ionic conductivities; therefore, the reversibility of fluorination/defluorination would be declined via charging the adequately deep Bi from the surface. Figure 4(b) illustrates the charge–discharge profile of the Pb–Bi cell, i.e., no PbF_2 exists on the surface of the negative electrode. In this cell, even a subtle charge–discharge reaction did not occur, and the electrode had a capacity of equal to or less than approximately 10 nAh. Thus, the charge reaction of FSB was in need for fluoride species, such as the PbF_2, on the negative electrode. As expected, the charge capacity and number of cycles significantly increased with an increase in the initial capacity of PbF_2 on the negative electrode from 0.1 to 1.0 mAh depicted in Figure 4(c) to 4(e)). In addition, Figure S5 illustrates the similar charge–discharge profiles using TMAF/TMPA-TFSA as the electrolyte solution. The same tendency as for MPPF/TMPA-TFSA

was confirmed, i.e., there was no significant difference between MPPF and TMAF. These results confirmed that this Pb|PbF_2–Bi FSB cell was charging based on a fluoride shuttle, that is, the defluorination of PbF_2 at the negative electrode and the fluorination of Bi at the positive one occurred simultaneously (Figure 4(a)). Next, the charge–discharge profile of the FSB cell with a PbF_2 capacity of 1.0 mAh on the negative electrode (Figure 4e) will be discussed.

In the charging process from the first to the sixth cycle, the FSB cell could be charged up to 0.1 mAh, despite the gradual increase in the overpotential. Beyond cycle 6, however, the charge capacity plummets. In contrast, the discharge profile exhibits two plateaus as described above, with discharge capacity being only 40–60% of that of the charge capacity, which gradually decreased with the number of cycles. Here, we compare the charge–discharge profile with that of the case in which the FSB cell charged all at once to the reactive limit in depth as demonstrated in the previous paper.[24] The results are displayed in Figure S6. In this comparison, both galvanostatic charge–discharge tests were performed at half the current density in Figure 4, i.e., 5 μA/cm^2.

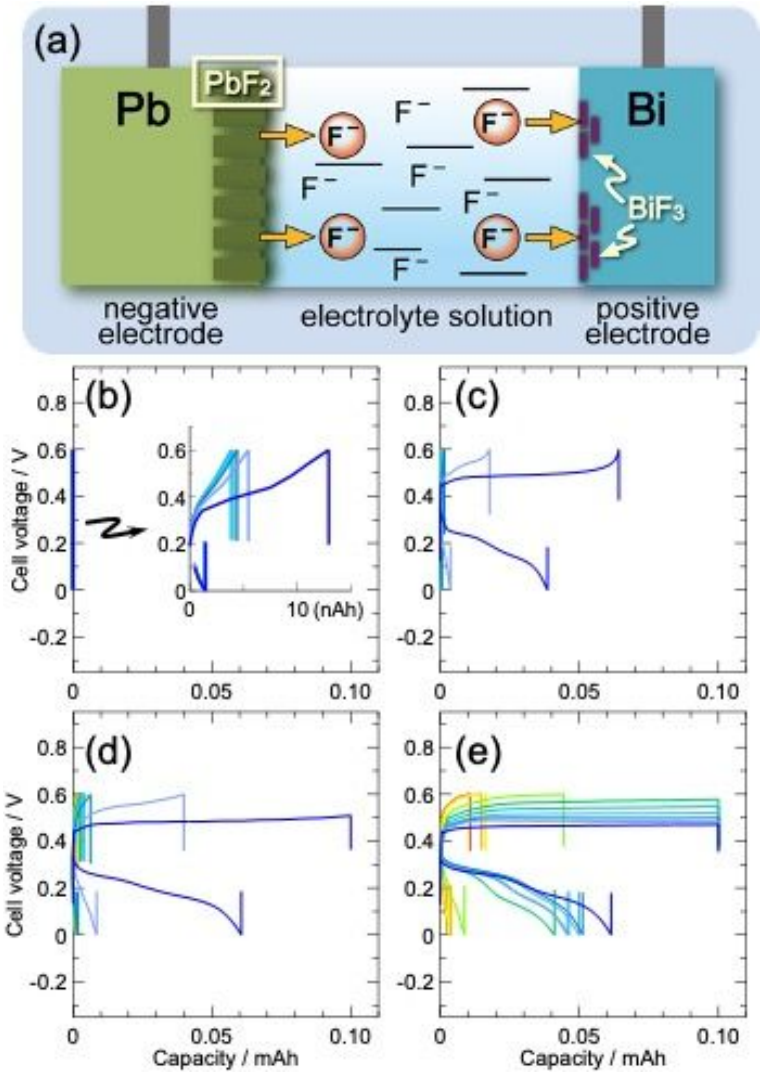

Figure 4. (a) Schematic of the Pb|PbF_2–Bi FSB system during the charge process. (b–e) Charge–discharge curves of the Pb|PbF_2–Bi FSB system with various initial capacities of PbF_2 on the Pb|PbF_2 negative electrode: (b) 0, (c) 0.1, (d) 0.2, and (e) 1.0 mAh, respectively.

As illustrated in Figure S6(a), although the FSB cell was charged up to 0.3 mAh at the initial charge reaction, its capacity significantly degraded from the second cycle. In contrast, in the

charge–discharge test limited at a charge capacity of 0.1 mAh (Figure S6(b)), the FSB cell could be charged up to the sixth cycle with an increase in the overpotential, as anticipated. A charge capacity of 0.3 mAh corresponds to a fluorination reaction that has progressed to a depth of 3.2 μm from the surface of the Bi plate electrode, as calculated from the bulk metal density and projected area of the electrode. We hypothesize that the formation of BiF_3 to such a depth, which exhibits poor ionic and electronic conductivities, would greatly impede the reversibility of the fluorination/defluorination reaction. In fact, the utilization of only 40–60% in the discharge reaction suggests the accumulation of isolated and inactive BiF_3 (dead BiF_3) on the surface in each cycle. This indicates that the progress of subsequent fluorination (charge reaction) in a deeper layer in Bi. To confirm this conjecture, we analyzed the *in situ* EC-AFM measurements of the morphological changes of Bi and Pb during fluorination/defluorination, which constitute the positive and negative electrodes of the FSB cell, respectively. The *in situ* EC-AFM measurements were performed using the airtight cell as shown in Figure S1. The reason for using it was to avoid reactions between the fluoride-containing electrolyte solution and water vapor in the air. If these reacted, the fluoride species readily change to $(HF)_nF^-$, and the $TMPA^+$ cation would be

progressively decomposed by the Hofmann elimination. Therefore, it was necessary to use the airtight *in situ* EC-AFM cell for the fluoride-containing electrolyte solution.

Figure 5 displays the snapshots of a video on the time-dependent topological variation of the surface of the Bi plate during fluorination in TMAF/TMPA-TFSA. The original video is provided as Movie 1 in the Supporting Information section. Here, the measurement points were marginally shifted between images (a) and (b) for ease of viewing the surface changes. The Bi plate was fluorinated once, and then a bare surface with a few fluorinated points was selected. Yellow arrows in each figure indicate upheaved regions. As the galvanostatic fluorination progressed, cracks appeared on the flat Bi surface, and propagated from the first point in the upheaved region. The cracks were presumed to occur along the grain boundary of the Bi plate. The upheaval was caused by the large volume change, expansion, during the conversion from Bi to BiF_3. Consequently, the electrolyte solution, i.e., an active fluoride species could penetrate deeper into the surface of Bi formed by exfoliation of the upheaved planes.

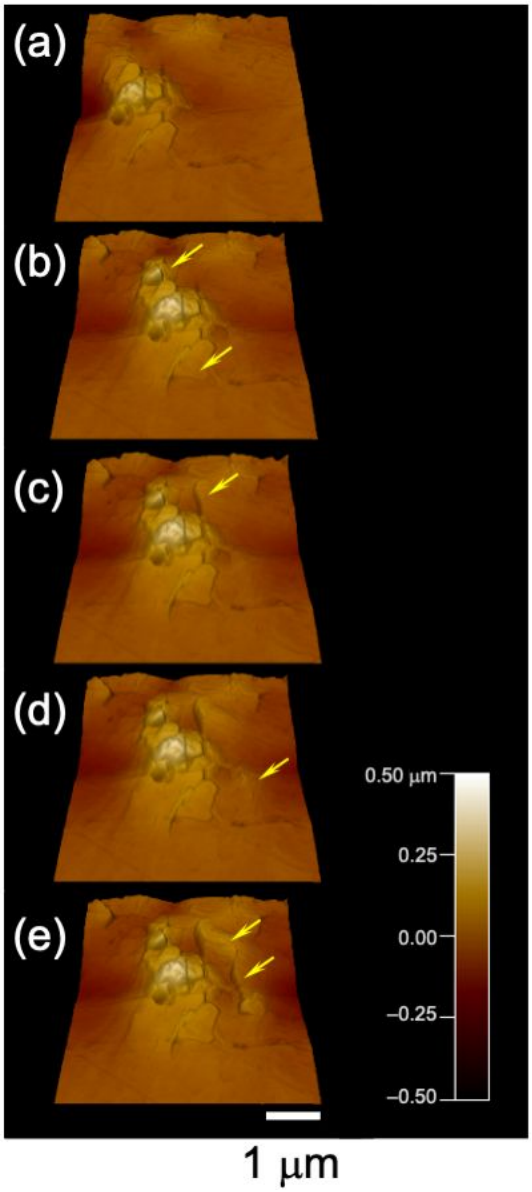

Figure 5. Time-dependent topological variation of the surface of the Bi plate during galvanostatic fluorination in TMAF/TMPA-TFSA as obtained by *in situ* EC-AFM. The measurement points are purposely shifted between (a) and (b) for a clearer view of the surface changes. Yellow arrows indicate the upheaved regions.

In the previous study, we captured SEM images of the fluorinated surface of Bi after the first charge; the entire surface was covered in upheaved BiF_3.[24] Thus, the current *in situ* EC-AFM observation clearly demonstrated the topological change of the Bi positive electrode in the charging process of the Pb|PbF_2–Bi FSB. In addition, Movies 2 and 3 (Supporting Information) play the results of the *in situ* EC-AFM observation during the defluorination and re-fluorination of the Bi electrode following Movie 1. The outermost upheaved layer had remained intact after defluorination, while the lower upheaved layer gradually receded (Movie 2). In subsequent fluorination (re-fluoridation) at the same region, the deeper layer re-emerged, and the surface became rougher (Movie 3). Thus, we demonstrated via *in situ* EC-AFM measurements that isolated and inactive BiF_3 accumulates on the topmost surface in each cycle. Generally, the problem of the isolated and inactive BiF_3 is easily overcome by the BiF_3/C composite electrode composed of BiF_3 powder with a suitably small particle diameter.

The morphological change trend of Pb was unlike that of Bi. Figure 6 displays snapshots of the video on the time-dependent topological change of the surface of the Pb plate during its fluorination in TMAF/TMPA-TFSA. The original video is presented as Movie 4 in Supporting Information. In this measurement, we selected a region on the bare surface with a few fluorinated

points after one cycle of fluorination. As the fluorination progressed, PbF_2 crystals appeared abruptly at arbitrary positions to a notably large size at this resolution. The yellow arrows in the figures indicate the crystal nuclei formed at the surface. The nuclei grow on the surface after formation.

For example, the crystal nuclei at the top edge in Figure 6(a) burgeons over time. In addition, after sometime, the newly generated crystal nuclei were larger than the early ones. Here, as is clear from the CV and XRD patterns illustrated in Figure 2, the fluorination of Pb is preceded by dissolution. These facts suggest that the crystal nuclei had already grown in the electrolyte solution before deposition onto the Pb surface. That is, the unexpected formation of the crystal nuclei at arbitrary locations observed in the *in situ* EC-AFM measurements of the Pb surface was presumed to be the result of the following two-step reaction.

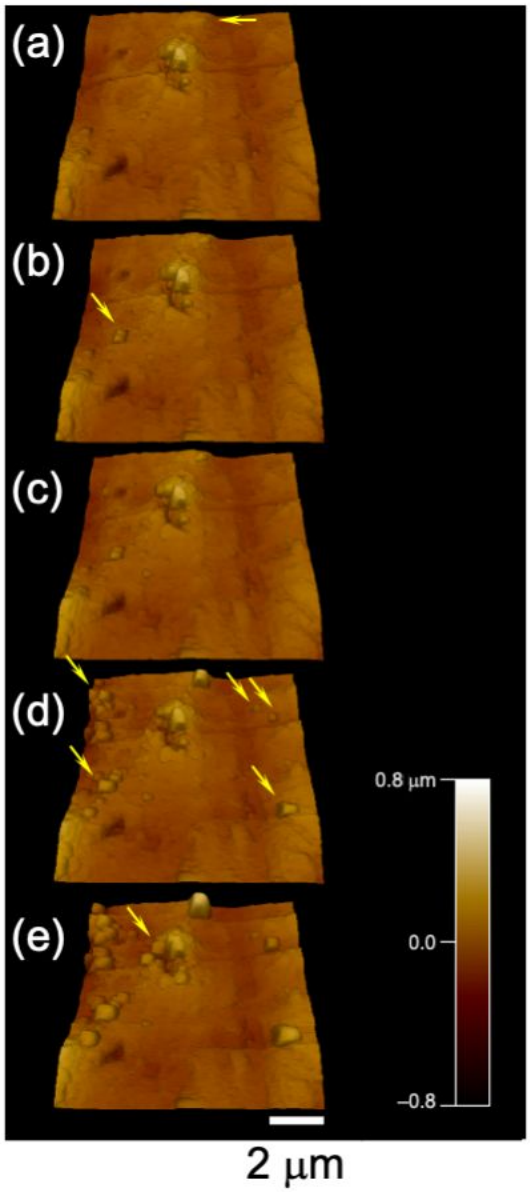

Figure 6. Time-dependent topological change of the surface of the Pb plate during fluorination in TMAF/TMPA-TFSA as obtained by *in situ* EC-AFM. Yellow arrows indicate the abruptly formed crystal nuclei.

The Pb^{2+} ions dissolved as the initial step of the sequential fluorination reacted with the F^- ions in the electrolyte solution to form PbF_2 nanoparticles (crystal nuclei), which were deposited on the Pb plate at some time. Consequently, the location of the formation of PbF_2 crystal nuclei was arbitrary, and hence unpredictable. Once the PbF_2 crystal nuclei was deposited on the Pb plate, the two reactions, $Pb \rightarrow Pb^{2+} + 2e^-$ (dissolution) and $Pb^{2+} + 2F^- \rightarrow PbF_2$ (deposition), proceeded simultaneously at the interface between the bare Pb surface and the PbF_2 crystal nucleus. Consequently, the buried PbF_2 crystal formed as displayed in Figure 2(c), (d) and Figure S3. This reaction mechanism, in which the active material is dissolved followed by deposition, is likely to cause aggregation and desorption of the active material on/from the composite electrode. Additionally, deposition on the opposite electrode is also a concern.

The reason for the poor cycling performance of the Pb|PbF_2–Bi FSB cell is not only the isolation of BiF_3 formed during the charging process, but also the dissolution–deposition mechanism of Pb. In fact, no studies have reported the construction of two-electrode rechargeable batteries using positive and negative electrodes based on the fluoride shuttle phenomenon in an electrolyte solution, in which the dissolution–deposition mechanism is used as the electrode reaction for the active materials. In addition, to the best of the authors' knowledge, no chargeable–dischargeable

FSB cell using an electrolyte solution has been demonstrated. To develop FSBs that can be operated at room temperature using an electrolyte solution, researchers must design active materials that promote reactions near their surfaces without being dissolved in the electrolyte solution, e.g., Bi in Figure 5. They must further design the effective components that constitute the electrolyte solution. We are currently working on further improvements to the FSB in this direction.

4. Conclusions

In conclusion, we report that morphological changes of active materials, Bi and Pb for the solution-based FSB, at their interface with an electrolyte solution were investigated by *in situ* EC-AFM measurement for the first time. Difference in the morphological changes of the active material surface between two mechanisms, direct fluorination and dissolution–deposition, were explained with evidence. In direct fluorination, large structural changes propagating on the surface, clacks and upheavals, were observed during conversion of metal into metal-fluoride. In dissolution–deposition, the crystal nuclei of the products, metal fluoride, were formed in the electrolyte solution and then deposited on the original metal surface, and subsequently grew. The location of the crystal nuclei deposited on the surface was arbitrary, and hence unpredictable.

Therefore, the position and degree of fluorination and defluorination cannot be controlled in an electrode with the dissolution–deposition mechanism, i.e., the process is not reversible. Thus, the main causes of the fading of cyclability in FSBs using electrolyte solutions were identified. This work is anticipated to inspire interest in modifying electrolyte solutions and its additives, and designing structures of active materials, the FSB based on electrolyte solutions will be further improved.

ASSOCIATED CONTENT

Supporting Information.

Supplemental Figures S1, S2, S3, S4, S5 and S6 showing *in situ* EC-AFM setup, the results of EDS analyses of the surface of fluorinated Pb, magnified SEM image of the fluorinated Pb, XRD patterns of BiF_3/C depending on the time of milling, galvanostatic charge–discharge profiles of Pb|PbF_2–Bi FSB cell using TMAF/TMPA-TFSA, and comparison of the charge–discharge profiles of Pb|PbF_2–Bi FSB cell with and without cut off at 0.1 mAh for the charge capacity. Supplemental Movies 1, 2, 3, and 4 showing *in situ* EC-AFM observation during fluorination, defluorination, and re-fluorination of Bi, and fluorination of Pb.

AUTHOR INFORMATION

Corresponding Author

* Ken-ichi Okazaki

Office of Society-Academia Collaboration for Innovation, Kyoto University, Gokasho, Uji 611-0011, Japan; E-mail: k-okazaki@saci.kyoto-u.ac.jp.

ORCID

Ken-ichi Okazaki: 0000-0003-0800-712X

Toshiro Yamanaka: 0000-0001-5784-0025

Author Contributions

K.O. performed the experiments and wrote the manuscript. H.N. performed the ^{19}F-NMR measurements and discussed the whole results. All authors have given approval to the final version of the manuscript.

Notes

The authors declare no competing financial interest.

ACKNOWLEDGMENT

The authors are grateful to Dr. Reiji Takekawa for the measurement of ^{19}F-NMR. The authors thank to Ms. Tomomi Yamamoto for her technical assistance during the experiments. The authors also thank to Mr. Masahiro Shiota and Mr. Yuki Saeki for their technical assistance during the experiments. This work is based on results obtained from projects, "Research and Development Initiative for Scientific Innovation of New Generation Batteries" (RISING, RISING2 & RISNG3; JPNP09012, JPNP16001 & JPNP21006), commissioned by the New Energy and Industrial Technology Development Organization (NEDO).

REFERENCES

(1) Armand, M.; Tarascon, J.M. Building better batteries. *Nature* 2008, *451*, 652-657.

(2) Nitta, N.; Wu, F.X.; Lee, J.T.; Yushin, G. Li-ion battery materials: present and future. *Mater. Today* 2015, *18*, 252-264.

(3) Wu, F.X.; Maier, J.; Yu, Y. Guidelines and trends for next-generation rechargeable lithium and lithium-ion batteries. *Chem. Soc. Rev.* **2020,** *49*, 1569-1614.

(4) Hua, X.; Eggeman, A.S.; Castillo-Martinez, E.; Robert, R.; Geddes, H.S.; Lu, Z.H.; Pickard, C.J.; Meng, W.; Wiaderek, K.M.; Pereira, N.; Amatucci, G.G.; Midgley, P.A.; Chapman, K.W.; Steiner, U.; Goodwin, A.L.; Grey, C.P. Revisiting metal fluorides as lithium-ion battery cathodes. *Nat. Mater.* **2021,** *20*, 841-850.

(5) Zhao, X.; Zhao-Karger, Z.; Wang, D.; Fichtner, M. Metal Oxychlorides as Cathode Materials for Chloride Ion Batteries. *Angew. Chem. Int. Ed.* **2013,** *52*, 13621-13624.

(6) Zhao, X.Y.; Zhao-Karger, Z.; Fichtner, M.; Shen, X.D. Halide-Based Materials and Chemistry for Rechargeable Batteries. *Angew. Chem.-Int. Edit.* **2020,** *59*, 5902-5949.

(7) Li, Z.Y.; Vinayan, B.P.; Jankowski, P.; Njel, C.; Roy, A.; Vegge, T.; Maibach, J.; Lastra, J.M.G.; Fichtner, M.; Zhao-Karger, Z. Multi-Electron Reactions enabled by Anion-Based Redox Chemistry for High-Energy Multivalent Rechargeable Batteries. *Angew. Chem.-Int. Edit.* **2020,** *59*, 11483-11490.

(8) Karkera, G.; Anji Reddy, M.; Fichtner, M. Recent developments and future perspectives of anionic batteries. *J. Power Sources* **2021,** *481*, 17.

(9) Zhang, K.Q.; Jin, Z. Halogen-enabled rechargeable batteries: Current advances and future perspectives. *Energy Storage Mater.* **2022,** *45*, 332-369.

(10) Nowroozi, M.A.; Mohammad, I.; Molaiyan, P.; Wissel, K.; Anji Reddy, M.; Clemens, O. Fluoride ion batteries - past, present, and future. *J. Mater. Chem. A* **2021,** *9*, 5980-6012.

(11) Haruyama, J.; Okazaki, K.; Morita, Y.; Nakamoto, H.; Matsubara, E.; Ikeshoji, T.; Otani, M. Two-Phase Reaction Mechanism for Fluorination and Defluorination in Fluoride-Shuttle Batteries: A First-Principles Study. *ACS Appl. Mater. Interfaces* **2020,** *12*, 428-435.

(12) Gschwind, F.; Rodriguez-Garcia, G.; Sandbeck, D.J.S.; Gross, A.; Weil, M.; Fichtner, M.; Hoermann, N. Fluoride ion batteries: Theoretical performance, safety, toxicity, and a combinatorial screening of new electrodes. *J. Fluorine Chem.* **2016,** *182*, 76-90.

(13) Danto, Y.; Poujade, G.; Pistre, J.D.; Lucat, C.; Salardenne, J. A Pb|PbF2|BiF3|Bi Thin Solid Film Reversible Galvanic Cell. *Thin Solid Films* **1978,** *55*, 347-354.

(14) Anji Reddy, M.; Fichtner, M. Batteries based on fluoride shuttle. *J. Mater. Chem.* **2011,** *21*, 17059-17062.

(15) Nowroozi, M.A.; Wissel, K.; Rohrer, J.; Munnangi, A.R.; Clemens, O. LaSrMnO4: Reversible Electrochemical Intercalation of Fluoride Ions in the Context of Fluoride Ion Batteries. *Chem. Mat.* **2017,** *29*, 3441-3453.

(16) Thieu, D.T.; Hammad, M.; Bhatia, H.; Diemant, T.; Chakravadhanula, V.S.K.; Behm, R.J.; Kubel, C.; Fichtner, M. CuF2 as Reversible Cathode for Fluoride Ion Batteries. *Adv. Funct. Mater.* **2017,** *27*, 11.

(17) Zhang, D.T.; Yamamoto, K.; Wang, Y.C.; Gao, S.H.; Uchiyama, T.; Watanabe, T.; Takami, T.; Matsunaga, T.; Nakanishi, K.; Miki, H.; Iba, H.; Amezawa, K.; Maeda, K.; Kageyama, H.; Uchimoto, Y. Reversible and Fast (De)fluorination of High-Capacity Cu2O Cathode: One Step Toward Practically Applicable All-Solid-State Fluoride-Ion Battery. *Adv. Energy Mater.* **2021**, *11*, 2102285.

(18) Nakano, H.; Matsunaga, T.; Mori, T.; Nakanishi, K.; Morita, Y.; Ide, K.; Okazaki, K.; Orikasa, Y.; Minato, T.; Yamamoto, K.; Ogumi, Z.; Uchimoto, Y. Fluoride-Ion Shuttle Battery with High Volumetric Energy Density. *Chem. Mat.* **2021,** *33*, 459-466.

(19) Mohammad, I.; Witter, R.; Fichtner, M.; Anji Reddy, M. Room-Temperature, Rechargeable Solid-State Fluoride-Ion Batteries. *ACS Appl. Energ. Mater.* **2018,** *1*, 4766-4775.

(20) Mohammad, I.; Witter, R.; Fichtner, M.; Anji Reddy, M. Introducing Interlayer Electrolytes: Toward Room-Temperature High-Potential Solid-State Rechargeable Fluoride Ion Batteries. *ACS Appl. Energ. Mater.* **2019,** *2*, 1553-1562.

(21) Darolles, I.; Weiss, C.M.; Alam, M.M.; Tiruvannamalai, A.; Jones, S.C. Fluoride ion battery compositions. U.S. Patent, US20120164541 A1, Jun. 28, 2012.

(22) Weiss, C.M.; Jones, S.C.; Tiruvannamalai, A.; Darolles, I.; Alam, M.M.; Hossain, S. Fluoride ion battery electrolyte compositions. U.S. Patent, US20160181665 A1, Jun. 23, 2016.

(23) Gschwind, F.; Zao-Karger, Z.; Fichtner, M. A fluoride-doped PEG matrix as an electrolyte for anion transportation in a room-temperature fluoride ion battery. *J. Mater. Chem. A* **2014,** *2*, 1214-1218.

(24) Okazaki, K.; Uchimoto, Y.; Abe, T.; Ogumi, Z. Charge-Discharge Behavior of Bismuth in a Liquid Electrolyte for Rechargeable Batteries Based on a Fluoride Shuttle. *ACS Energy Lett.* **2017,** *2*, 1460-1464.

(25) Davis, V.K.; Bates, C.M.; Omichi, K.; Savoie, B.M.; Momcilovic, N.; Xu, Q.M.; Wolf, W.J.; Webb, M.A.; Billings, K.J.; Chou, N.H.; Alayoglu, S.; McKenney, R.K.; Darolles, I.M.; Nair, N.G.; Hightower, A.; Rosenberg, D.; Ahmed, M.; Brooks, C.J.; Miller, T.F.; Grubbs, R.H.; Jones, S.C. Room-temperature cycling of metal fluoride electrodes: Liquid electrolytes for high-energy fluoride ion cells. *Science* **2018,** *362*, 1144-1148.

(26) Konishi, H.; Minato, T.; Abe, T.; Ogumi, Z. Electrochemical Performance of a Bismuth Fluoride Electrode in a Reserve-Type Fluoride Shuttle Battery. *J. Electrochem. Soc.* **2017,** *164*, A3702-A3708.

(27) Konishi, H.; Minato, T.; Abe, T.; Ogumi, Z. Electrochemical properties of lead fluoride electrode in fluoride shuttle battery. *J. Electroanal. Chem.* **2018,** *826*, 60-64.

(28) Konishi, H.; Minato, T.; Abe, T.; Ogumi, Z. Influence of Electrolyte Composition on the Electrochemical Reaction Mechanism of Bismuth Fluoride Electrode in Fluoride Shuttle Battery. *J. Phys. Chem. C* **2019,** *123*, 10246-10252.

(29) Yamamoto, T.; Matsumoto, K.; Hagiwara, R.; Nohira, T. Room-Temperature Fluoride Shuttle Batteries Based on a Fluorohydrogenate Ionic Liquid Electrolyte. *ACS Appl. Energ. Mater.* **2019,** *2*, 6153-6157.

(30) Kawasaki, M.; Morigaki, K.; Kano, G.; Nakamoto, H.; Takekawa, R.; Kawamura, J.; Minato, T.; Abe, T.; Ogumi, Z. Lactone-Based Liquid Electrolytes for Fluoride Shuttle Batteries. *J. Electrochem. Soc.* **2021,** *168*, 010529.

(31) Shimoda, K.; Minato, T.; Konishi, H.; Kano, G.; Nakatani, T.; Fujinami, S.; Kucuk, A.C.; Kawaguchi, S.; Ogumi, Z.; Abe, T. Defluorination/fluorination mechanism of Bi(0.8)Ba(0.2)F2.8 as a fluoride shuttle battery positive electrode. *J. Electroanal. Chem.* **2021,** *895*, 115508.

(32) Yamamoto, T.; Matsumoto, K.; Hagiwara, R.; Nohira, T. Charge-Discharge Performance of Copper Metal Positive Electrodes in Fluorohydrogenate Ionic Liquids for Fluoride-Shuttle Batteries. *J. Electrochem. Soc.* **2021,** *168*, 6.

(33) Kawauchi, S.; Nakamoto, H.; Takekawa, R.; Kobayashi, T.; Abe, T. Electrolytes for Room-Temperature Rechargeable Fluoride Shuttle Batteries. *ACS Appl. Energ. Mater.* **2022,** *5*, 2096-2103.

(34) Yamanaka, T.; Okazaki, K.; Abe, T.; Nishio, K.; Ogumi, Z. Evolution of Reactions of a Fluoride Shuttle Battery at the Surfaces of BiF3 Microclusters Studied by InSitu Raman Microscopy. *ChemSusChem* **2019,** *12*, 527-534.

(35) Yamanaka, T.; Okazaki, K.; Ogumi, Z.; Abe, T. Reactivity and Mechanisms in Fluoride Shuttle Battery Reactions: Difference between Orthorhombic and Cubic BiF3 Single Microparticles. *ACS Appl. Energ. Mater.* **2019,** *2*, 8801-8808.

(36) Kumagae, K.; Okazaki, K.; Matsui, K.; Horino, H.; Hirai, T.; Yamaki, J.; Ogumi, Z. Improvement of Cycling Performance of FeF3-Based Lithium-Ion Battery by Boron-Based Additives. *J. Electrochem. Soc.* **2016,** *163*, A1633-A1636.

(37) Shenderovich, I.G.; Smirnov, S.N.; Denisov, G.S.; Gindin, V.A.; Golubev, N.S.; Dunger, A.; Reibke, R.; Kirpekar, S.; Malkina, O.L.; Limbach, H.H. Nuclear magnetic resonance of hydrogen bonded clusters between F- and (HF)(n): Experiment and theory. *Ber. Bunsen-Ges. Phys. Chem. Chem. Phys.* **1998,** *102*, 422-428.

(38) Sun, H.R.; DiMagno, S.G. Anhydrous tetrabutylammonium fluoride. *J. Am. Chem. Soc.* **2005,** *127*, 2050-2051.

Table of Contents